RSC Advances

PAPER

View Article Online
View Journal | View Issue

Cite this: *RSC Adv.*, 2022, **12**, 1471

Synthesis of bimetallic nickel cobalt selenide particles for high-performance hybrid supercapacitors†

Bei Jiang,[ab] Yang Liu,[ab] Jingchao Zhang,[b] Yinhuan Wang,[b] Xinyu Zhang,[b] Renchun Zhang,[b] Liang-Liang Huang *[a] and Daojun Zhang *[b]

Received 27th November 2021
Accepted 20th December 2021

DOI: 10.1039/d1ra08678b

rsc.li/rsc-advances

Supercapacitors are known as promising excellent electrochemical energy storage devices because of their attractive features, including quick charge and discharge, high power density, low cost and high security. In this work, a series of litchi-like Ni–Co selenide particles were synthesized *via* a simple solvothermal method, and the Ni–Co compositions were carefully optimized to tune the charge storage performance, charge storage kinetics, and conductivity for battery-like supercapacitors. Interestingly, the optimal sample $Ni_{0.95}Co_{2.05}Se_4$ exhibits a high capacity of 1038.75 F g^{-1} at 1 A g^{-1} and superior rate performance (retains 97.8% of the original capacity at 4 A g^{-1}). Moreover, an asymmetric supercapacitor device was assembled based on the $Ni_{0.95}Co_{2.05}Se_4$ cathode and activated carbon anode. The device of $Ni_{0.95}Co_{2.05}Se_4$//active carbon (AC) reveals a peak energy density of 37.22 W h kg^{-1}, and the corresponding peak power density reaches 800.90 W kg^{-1}. This work provides a facile and effective way to synthesize transition metal selenides as high-performance supercapacitor electrode materials.

1. Introduction

In recent years, with the depletion of fossil energy and the deterioration of the environment, the development of energy-efficient energy storage devices has become a hot research field.[1–6] Due to the high power density and long life span for supercapacitors, more and more attention has been paid to them by researchers.[7–12] Recently, transition metal selenide electrode materials have been extensively studied in the field of renewable energy for enhancing energy storage capabilities.[13–16] The energy gap of selenides is smaller than that of oxides and sulfides of the same family, so selenides generally show superior electrochemical properties. Compared with Co or Ni single metal selenides,[17,18] purposely designed binary metal selenide composites are an effective method to optimize electrode performance. For example, the $(Ni,Co)Se_2$ bimetallic selenide-composite nanostructure was prepared by Wang *et al.*, as a result, the $(Ni,Co)Se_2$/NiCo LDH delivers a high capacity of 170 mA h g^{-1} (1224 F g^{-1}) at a current density of 2 A g^{-1}.[19] The specific capacity of reported $NiCo_2Se_4$-rGO reaches 2038.55 F g^{-1} at a current density of 1 A g^{-1}, and maintains 90% of the original capacity after 1000 cycles.[20] Liu *et al.* designed and synthesized core–shell structure selenium-enriched bimetallic selenide balls as the battery–supercapacitor hybrid cathode electrode, the capacity of the electrode reaches 164.44 mA h g^{-1} at current density 1 A g^{-1}, and it still maintains 85.72% of the initial capacity after 5000 cycles.[21] Aside from considering the morphology effect on the electrochemical performance, control of the synergy between nickel and cobalt ions in the active material is another useful way to increase the capacitance.

The pyrite-type $NiCoSe_4$ is an ideal research model for supercapacitor, tuning of Ni/Co ratio in the structure may be an effect way to improve the sluggish kinetics.[22] The $NiCo_{2.1}Se_{3.3}$-NSs array electrode material with high conductivity and excellent specific capacitance of 742.4 F g^{-1} under 1 mA cm^{-2} was prepared by Wang *et al.*, and still maintained 83.8% of the original capacity after 1000 cycles.[23] In the all above reports, due to the good synergy between nickel and cobalt ions, the electrochemical performances of Co–Ni selenides have prominent advantages than single metal selenides, and according to current reports, researchers are often devoted to development of different structure materials to act as cathode materials for supercapacitor devices, however, rarely optimized Ni/Co compositions of Ni–Co–selenide carefully to tune charge storage performances for supercapacitor.

In this work, we present a simple one step solvothermal method to prepare spherical particles of Ni–Co–selenide with different ratios of nickel and cobalt ions, and the electrochemical properties of this series of products were studied.

[a]*School of Chemistry and Material Science, Liaoning Shihua University, Fushun 113001, Liaoning, P. R. China. E-mail: huangll@lnpu.edu.cn*

[b]*College of Chemistry and Chemical Engineering, Anyang Normal University, Anyang 455000, Henan, China. E-mail: zhangdj0410@sohu.com; Tel: +86 372 2900040*

† Electronic supplementary information (ESI) available: Size distribution of the of bimetallic nickel cobalt selenide particles, EDX spectrometography of these samples, SEM spectrometography of different samples. Co_3Se_4, $Ni_{1.14}Co_{1.86}Se_4$, $Ni_{0.67}Co_{2.33}Se_4$, $Ni_{0.53}Co_{2.47}Se_4$. CV, GCD curves, and Nyquist plot of Co_3Se_4 and $Ni_{0.53}Co_{2.47}Se_4$. See DOI: 10.1039/d1ra08678b

Surprisingly, the optimized $Ni_{0.95}Co_{2.05}Se_4$ particles as supercapacitor electrode shows the highest capacity and distinguished cycling stability. Besides, the as-fabricated hybrid supercapacitor device ($Ni_{0.95}Co_{2.05}Se_4$//AC) composed of selenide positive electrode and activated carbon negative electrode exhibits 45.86 mA h g^{-1} (104.68 F g^{-1}) at 1 A g^{-1} and retains 95.21% of initial capacitance after 4000 cycles.

2. Experimental

2.1 Material preparation

Cobalt(II)2,4-pentanedionate, nickel(II)2,4-pentanedionate, cyclohexane, ethylene glycol, *N*,*N*-dimethylformamide (DMF), *N*-methyl-2-pyrrolidone (NMP), polyvinylidene fluoride (PVDF), polytetrafluoroethylene (PTFE), and graphite powder were purchased from Sinopharm Chemical Reagent Co, Ltd. All chemical reagents used in this work are analytically pure and are not further purification.

2.2 Synthetic active material

Firstly, the total amount of 0.1 mmol mixture of nickel(II)2,4-pentanedionate and cobalt(II)2,4-pentanedionate and equal amounts of sodium selenide were added to the 20 mL Teflon autoclave. 2.5 mL of DMF, 6.0 mL of water, 0.5 mL of cyclohexane and 3.0 mL of ethylene glycol were then added in turn to stir on the magnetic agitator for an hour. The resulting uniform mixture solution was placed in an oven and kept for 12 h at 180 °C. Black solid products were washed three times with ethanol and deionized water and dried at 80 °C for 8 h. Under the same operating conditions, we also synthesized other samples of nickel–cobalt selenide with Ni/Co molar ratios of 0 : 1,1 : 2, 1 : 2.2, 1 : 4 and 1 : 5.

2.3 Electrode production

The as-prepared black solid samples, PVDF, and acetylene black in accordance with the ratio of 8 : 1 : 1 in the mortar of mixed grinding, then adding 120 μL of NMP to grind into an ink-like black solution. The ink was evenly coated on a 1 × 1 cm^2 nickel foam and then pressed at 10 MPa. Finally, a cathode electrode was obtained after vacuum-dried at 110 °C for 12 h. The manufacturing method of other sample electrodes is the same as above. The difference is that when assembling asymmetric supercapacitors, anode electrode plate was prepared *via* mixed with activated carbon, PTFE, and acetylene black in 8 : 1 : 1 ratio and evenly coated on nickel foam.

2.4 Electrochemical measurement

The electrochemical tests of these nickel–cobalt selenides modified electrodes were conducted on an electrochemical workstation (CHI 660E) at room temperature by three-electrode system in 2 M KOH solution. The Hg/Hg_2Cl_2 electrode was used as the reference electrode and the Pt foil was used as the counter electrode, respectively. The specific capacitance of electrodes can be calculated according to GCD curves under the three-electrode system by using the following equation.[24]

$$C = \frac{i\Delta t}{m\Delta V}\left(\mathrm{F\ g^{-1}}\right) \quad (1)$$

where, Δt is discharge time (s), i is the applied current in density (A), ΔV is the voltage change in the discharge process, and m is the mass of active material of the working electrode (g). The overall electrode samples preparation, fabrication and three-electrode measurements process was displayed in Scheme 1.

2.5 Electrochemical performance of hybrid supercapacitor (HSC) device

In order to study the electrochemical properties of the optimized electrode, it is assembled into asymmetric supercapacitors with active carbon as negative. The useful area of the positive and negative electrodes is 1 × 1 cm^2. The mass selection of the two electrodes is calculated according to the theory of charge balance ($Q_+ = Q_-$) (eqn (2)).

$$Q_+ = Q_- = \frac{m_+}{m_-} = \frac{C_- \times \Delta V_-}{C_+ \times \Delta V_+} \quad (2)$$

where C refers to the specific capacitance (F g^{-1}), ΔV represents the potential window (V), and m indicates the mass of the electrode material on both the positive and negative electrodes (g).[25] For HSC, energy density (E), and power density (P) can be calculated using eqn (3) and eqn (4).

$$E = \frac{1}{2 \times 3.6} \times C \times \Delta V^2 \ \left(\mathrm{W\ h\ kg^{-1}}\right) \quad (3)$$

$$P = \frac{3600 \times E}{\Delta t} \ \left(\mathrm{W\ kg^{-1}}\right) \quad (4)$$

where Δt is the discharge time (s), and ΔV is the applied potential window (V).[26,27]

3. Results and discussion

In the one-step solvothermal synthesis of nickel–cobalt selenide particles, cobalt acetylacetonate and nickel acetylacetonate at the molar ratio of 0 : 1, 1 : 2, 1 : 2.2, 1 : 4 and 1 : 5 to obtain a series of nickel cobalt selenides ($Ni_xCo_{3-x}Se_4$). There was no significant difference in the morphology of the nickel–cobalt selenide particles, and their average diameters were around 191 to 243 nm, the detailed data is shown in Fig.S1, S2, and Table

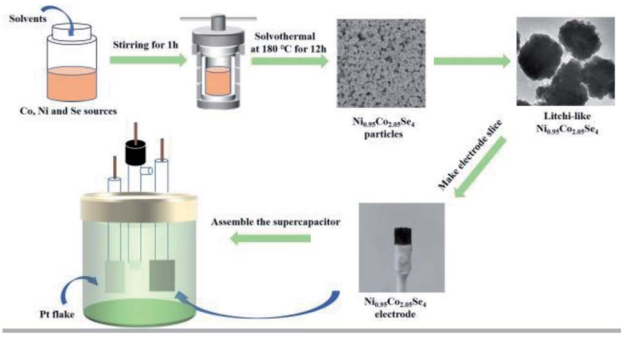

Scheme 1 Schematic illustration for the synthesis of electrode materials and assemble the supercapacitor.

S1.† Fig. 1a shows the XRD patterns of the as-synthesized products at different proportions. The XRD peaks of pure Co_3Se_4 sample match well with the monoclinic phase Co_3Se_4 (ref. 28) with the PDF no. of 96-901-2804. With the increase of the content of nickel ions, the intensity of the diffraction peak remained unchanged, and the peak position shifted to left slightly. According to the Bragg equation $2d\sin\theta = n\lambda$, the radius of the metal nickel ions is larger than the radius of the cobalt ions, and this causing a slight negative shift of the diffraction peak in the Ni-doped products, the main diffraction peak of $Ni_{1.14}Co_{1.86}Se_4$ at 33.2° matches well with the monoclinic Ni_3Se_4 (18-0890). Furthermore, the FWHM is inversely proportional to particle size, thus the pure Co_3Se_4 demonstrates the smallest particle size, the consequence is consistent with the statistical result shown in Fig. 1b. EDX analysis showed that the distribution of elements in each product was uniform and the proportion was close to the theoretical value (Fig. S3†). The calculated chemical formula of the synthesized samples is Co_3Se_4, $Ni_{1.14}Co_{1.86}Se_4$, $Ni_{0.95}Co_{2.05}Se_4$, $Ni_{0.67}Co_{2.33}Se_4$, and $Ni_{0.53}Co_{2.47}Se_4$, respectively.

As shown in Fig. 2a and b, SEM images of $Ni_{0.95}Co_{2.05}Se_4$ sample show that the particles were uniform distributed without impurities, which allows the active material to be evenly distributed on the electrode surface to improve electrochemical properties. The growth mechanism of $Ni_{0.95}Co_{2.05}Se_4$ sample was furthermore studied at different conditions. The SEM images of different synthesis temperatures and times are shown in Fig. S4a–h and S4i–p,† it clearly seen that low temperature and short-term reaction time have a great influence on the morphology. It is difficult to form at a low temperature of 100 °C even the reaction time till to 12 h, while reaction temperature reaches 160 °C, the yield is low in reaction time of 1 h. In addition, we have further studied the influence of reagent dosage on the morphology as shown in Fig. S5a–f.† Sample morphology with the absence of cyclohexane (Fig. S5a and b†), ethylene glycol (Fig. S5c and d†) and both (Fig. S5e and f†) will cause adhesion and aggregation (Fig. S5g and h†), which shows that a small amount of cyclohexane and ethylene glycol can maintain a uniform morphology. When change Ni/Co ratio to 2.2 : 1, the octahedron morphology can be obtained (Fig. S5g and h†). TEM images of $Ni_{0.95}Co_{2.05}Se_4$ were further used to study the structure. The results are shown in Fig. 2c and d, which shows that the particles are about 194 nm solid

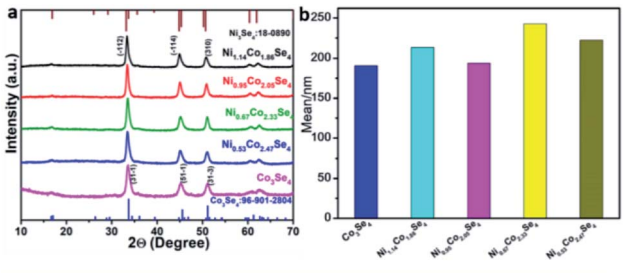

Fig. 1 (a) XRD patterns and (b) size distribution patterns of different samples.

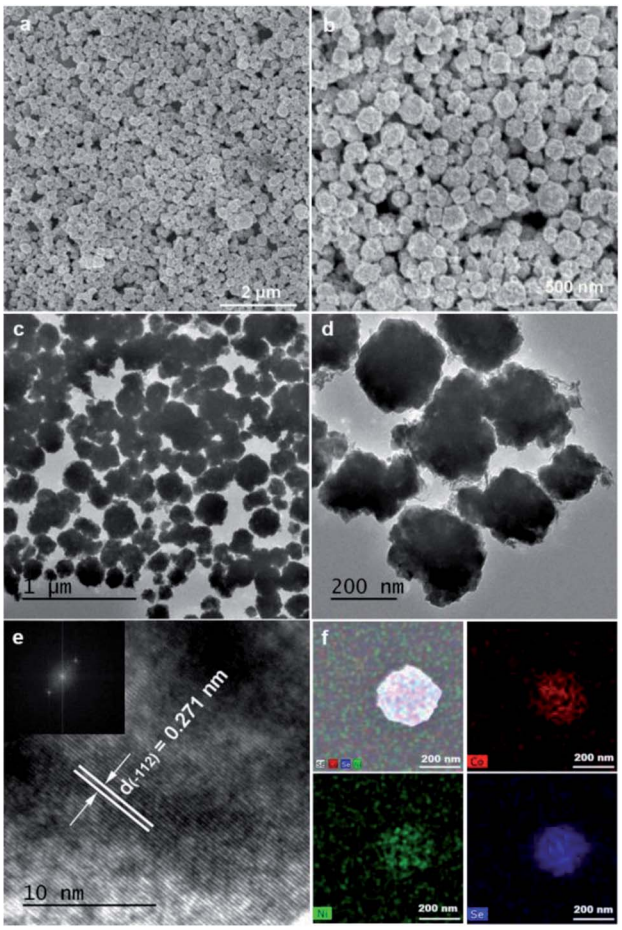

Fig. 2 (a and b) SEM images of $Ni_{0.95}Co_{2.05}Se_4$, (c and d) TEM images of $Ni_{0.95}Co_{2.05}Se_4$, (e) HRTEM image of the $Ni_{0.95}Co_{2.05}Se_4$, and (f) the corresponding elemental mapping images for Co, Ni, and Se of a single $Ni_{0.95}Co_{2.05}Se_4$ nanoparticle.

architecture, and the lattice fringes of $Ni_{0.95}Co_{2.05}Se_4$ sample can be clearly observed in high resolution TEM image (Fig. 2e). The lattice stripe spacing of 0.271 nm corresponds to the (−112) planes of Ni_3Se_4. Fig. 2f shows uniform distribution of Ni, Co, and Se elements in the sample of $Ni_{0.95}Co_{2.05}Se_4$. The nitrogen sorption isotherms and the pore size distribution of five Ni_x-$Co_{3-x}Se_4$ samples with different ratios are shown in Fig. S6.† The BET specific surface area of $Ni_{0.95}Co_{2.05}Se_4$ nanoparticles is 22.17 $m^2\ g^{-1}$, where the presence of mesopores can be determined. However, the BET area of Co_3Se_4, $Ni_{1.14}Co_{1.86}Se_4$, $Ni_{0.67}Co_{2.33}Se_4$, and $Ni_{0.53}Co_{2.47}Se_4$ is 15.92 $m^2\ g^{-1}$, 12.64 $m^2\ g^{-1}$, 9.0 $m^2\ g^{-1}$, and 9.57 $m^2\ g^{-1}$, respectively, which are all smaller than the $Ni_{0.95}Co_{2.05}Se_4$ sample. It is clearly found that mean mesoporous size of $Ni_{0.95}Co_{2.05}Se_4$ are smaller than others in the Fig. S6.† These data indicating that $Ni_{0.95}Co_{2.05}Se_4$ particle has more active sites and a larger contact area with the electrolyte than other samples.

X-Ray photoelectron spectroscopy (XPS) is used to analyze the surface element constitution and electronic state of the $Ni_{0.95}Co_{2.05}Se_4$ sample. Fig. 3a shows the survey scan spectrum of $Ni_{0.95}Co_{2.05}Se_4$ sample, which exhibits the chemical states of

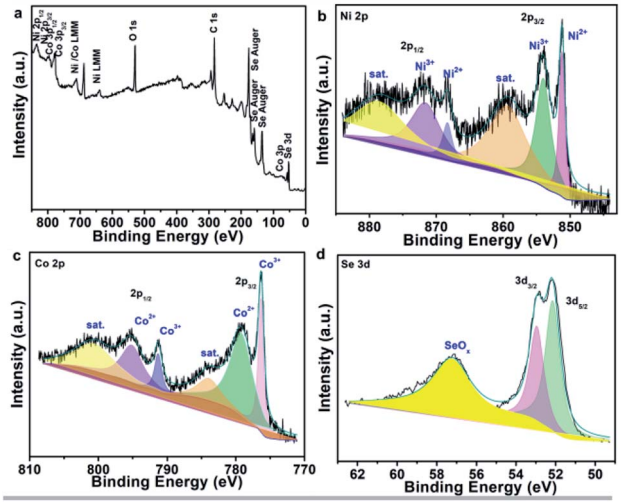

Fig. 3 XPS spectra of $Ni_{0.95}Co_{2.05}Se_4$ (a) wide-scan survey spectrum, (b) Ni 2p, (c) Co 2p, and (d) Se 3d spectra.

Ni 2p, Co 2p, and Se 2p.[29] After Gaussian fitting, three sets of peaks can be obtained from the 2p map of Ni, corresponding to two spin orbital peaks and two shake-up satellites. The peaks at 868.44 and 851.18 eV represent $2p_{3/2}$ and $2p_{1/2}$ of Ni^{2+}, respectively (Fig. 3b). Besides, the peaks at 854.13 and 871.88 eV are attributed to $2p_{3/2}$ and $2p_{1/2}$ of Ni^{3+} in $Ni_{0.95}Co_{2.05}Se_4$ particles.[30–32] The peaks with binding energies of 795.15 and 779.28 eV in Fig. 3c correspond to Co^{2+}, while the peaks located at 791.22 and 776.40 eV correspond to Co^{3+}. Moreover, there are two distinct satellite peaks located in the combined energy of 800.76 and 783.84 eV.[33–35] For the Se 3d spectra (Fig. 3d), there is a pair of metal-selenium bonds, which indicates the presence selenium ions in $Ni_{0.95}Co_{2.05}Se_4$ nanoparticles. The broad peak situated at 57.24 eV reflects surface Se species with a high oxidation state (SeO_x),[36,37] which is attributed to a small amount of oxidation on the surface.

Using 2 M KOH aqueous solution as the electrolyte, the electrochemical properties of the working electrodes for supercapacitors were tested in a three-electrode system. Fig. S7† shows CV curves of Co_3Se_4, $Ni_{1.14}Co_{1.86}Se_4$, $Ni_{0.95}Co_{2.05}Se_4$, $Ni_{0.67}Co_{2.33}Se_4$, and $Ni_{0.53}Co_{2.47}Se_4$ samples at a scanning speed of 20 mV s^{-1}. The curve of as-synthesized $Ni_{0.95}Co_{2.05}Se_4$ exhibited the strongest redox peaks and largest closed area among the five samples. In Fig. S8,† obviously, the sample of $Ni_{0.95}Co_{2.05}Se_4$ reveals the longest discharge time of the five electrodes, shows the best capacitance properties, which demonstrates the content of Ni/Co ratios has great influence on discharge capacity. Especially, the $Ni_{0.95}Co_{2.05}Se_4$ delivers a capacity of 1038.75 F g^{-1} at a current density of 1 A g^{-1}, while the corresponding capacity of Co_3Se_4, $Ni_{1.14}Co_{1.86}Se_4$, $Ni_{0.67}Co_{2.33}Se_4$, and $Ni_{0.53}Co_{2.47}Se_4$ samples is 512.06, 762.74, 760.04, and 734.81 F g^{-1}, respectively (Fig. S9†).

After comparing discharge curves of five different electrodes at 1 A g^{-1}, it is concluded that the $Ni_{0.95}Co_{2.05}Se_4$ electrode has the greatest energy storage capacity. Fig. 4a depicts the CV curves of $Ni_{0.95}Co_{2.05}Se_4$ at different scan rates (5–50 mV s^{-1})

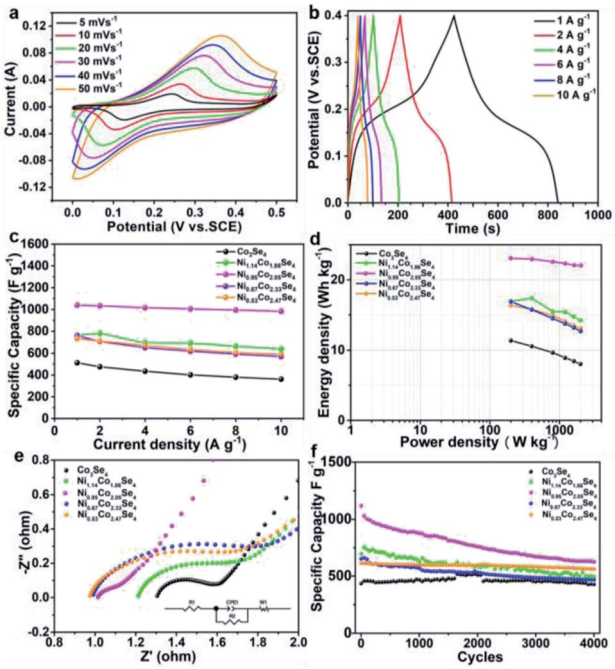

Fig. 4 (a) CV curves of $Ni_{0.95}Co_{2.05}Se_4$ at different scan rates, (b) GCD curves of $Ni_{0.95}Co_{2.05}Se_4$ electrode at various current densities, (c) specific capacity values of the electrodes *vs.* discharge current density, (d) energy density and power density diagram of different samples, (e) Nyquist plot of $Ni_{1.14}Co_{1.86}Se_4$, $Ni_{0.95}Co_{2.05}Se_4$, $Ni_{0.67}Co_{2.33}Se_4$, and (f) capacitance retention after 4000 consecutive charge–discharge cycles.

under operating potential of 0–0.5 V. As the scan rate increased, the shape of these curves showed negligible changes but the intensity of these curves is increased. Therefore, the $Ni_{0.95}Co_{2.05}Se_4$ electrode demonstrated fast electronic/ionic transport and high-rate capability. The GCD profiles of $Ni_{0.95}Co_{2.05}Se_4$ in Fig. 4b exhibit quasi-symmetric shaped curves, indicating reversible redox reaction during the charging and discharging process. The specific capacities of the series of electrodes were calculated from the discharge time in the GCD curves and shown in Fig. 4c, remarkably, 94.58% of the initial capacitance could be retained for $Ni_{0.95}Co_{2.05}Se_4$ electrode at a high current density of 10 A g^{-1}, which also exhibits a higher specific capacity and rate performance compared with other samples. The energy density and power density curves of the samples were calculated according to the discharge curves, which shows in Fig. 4d. In general, the value of P increases but E decreases with the increase of current density. The $Ni_{0.95}Co_{2.05}Se_4$ electrode can deliver a biggest energy density of 23.08 W h kg^{-1} at 1 A g^{-1} and the corresponding power density is 200.05 W kg^{-1}. The energy density still reaches 22.04 W h kg^{-1} when the power density reaches 1609.54 W kg^{-1}, and is higher than the energy density of the other samples.

The electrochemical impedance spectroscopy (EIS) of the nickel cobalt selenide series samples in the frequency range of 0.1 to 10^5 Hz are further studied. The Nyquist curves schematic of Co_3Se_4, $Ni_{1.14}Co_{1.86}Se_4$, $Ni_{0.95}Co_{2.05}Se_4$, $Ni_{0.67}Co_{2.33}Se_4$, and

$Ni_{0.53}Co_{2.47}Se_4$ electrode materials are shown in Fig. 4e, the shapes of these five samples are similar, a semicircle in the high frequency region represents the charge transfer resistance, and the straight line in the low frequency region represents the diffusion resistance, this corresponds to the Bode plot diagram in Fig. S10.† After fitting, these electrodes have the same equivalent circuit. It is clear seen that the introducing Ni ions in Co_3Se_4 lattice can effectively decrease the solution resistance (R_s). Due to the intrinsic half-metallic behavior, Co_3Se_4 exhibits small charge transfer resistance, as increasing Ni content to 32% in $Ni_{0.95}Co_{2.05}Se_4$, the R_{ct} decrease dramatically, indicating that the charge transfer speed is much faster.[38] Furthermore, according to the diffusion coefficient formula,[39] the diffusion coefficient value of $Ni_{0.95}Co_{2.05}Se_4$ is the largest among all the samples (Table S2†), this may be related to the effective diffusion of the OH^- in $Ni_{0.95}Co_{2.05}Se_4$ sample. Fig. 4f describes the cycling performance of the Co_3Se_4, $Ni_{1.14}Co_{1.86}Se_4$, $Ni_{0.95}Co_{2.05}Se_4$, $Ni_{0.67}Co_{2.33}Se_4$ and $Ni_{0.53}Co_{2.47}Se_4$ electrodes. The $Ni_{0.95}Co_{2.05}Se_4$ electrode exhibits a specific capacitance of 625.27 F g^{-1} (61.55% capacitance retention) after 4000 cycles at a current density of 4 A g^{-1}, whereas the others electrode exhibits a lower capacitance of 426.75, 493.47, 468.2, and 561.44 F g^{-1} after 4000 cycles at a current density of 4 A g^{-1}, respectively. Although the retention rate is not higher than other sample electrodes, the capacity after cycling is still higher than other capacity values. The $Ni_{0.95}Co_{2.05}Se_4$ electrode presents better electrochemical properties than some of the related supercapacitor electrode materials reported in the literature (Table S3†). Furthermore, the charge storage mechanism of the as-prepared series of electrode materials was investigated by fitting the plots of logarithmic anodic peak current *versus* logarithmic scan rate. According to the equation $\log(i) = b\log(v)+\log(a)$, the plot slope b of 0.5 and 1.0 is the contribution of the electrochemical process dominated by ionic diffusion and surface capacitive control process.[40] As shown in Fig. S11a,† the calculated b value of Co_3Se_4, $Ni_{1.14}Co_{1.86}Se_4$, $Ni_{0.95}Co_{2.05}Se_4$, $Ni_{0.67}Co_{2.33}Se_4$, and $Ni_{0.53}Co_{2.47}Se_4$ electrode is 0.795, 0.717, 0.707, 0.888, and 0.967, respectively, which indicated the diffusion contribution is dominant in $Ni_{0.95}Co_{2.05}Se_4$ electrode. The result is consistent with the 58% diffusion contribution of the capacitance at low scan speed of 10 mV s^{-1}, conversely, capacitive contribution enlarged at high rate for $Ni_{0.95}Co_{2.05}Se_4$ electrode (Fig. S11b†).

In order to further investigate the electrical properties of $Ni_xCo_{3-x}Se_4$ in practical applications, the HSC devices are assembled by using activated carbon as the negative electrode and the series of $Ni_xCo_{3-x}Se_4$ samples as the positive electrode. Fig. 5a displays the CV curves with a voltage window of −1.2–0 and 0–0.5 V for the activated carbon and $Ni_{0.95}Co_{2.05}Se_4$ electrodes at 5 mV s^{-1} in a three-electrodes system, respectively. The charge and discharge of the carbon electrode forms an approximately rectangular CV curve, and anodic active material exhibits a pair of strong redox peaks. Fig. S12a† shows the CV curves of 10 mV s^{-1} under different test ranges from 1.2–2.0 V. When the voltage range from 1.2 V to 1.4 V is selected, the corresponding Faraday effect is not reflected well, and when the voltage is further increased to 1.8 V and 2.0 V, the electrode

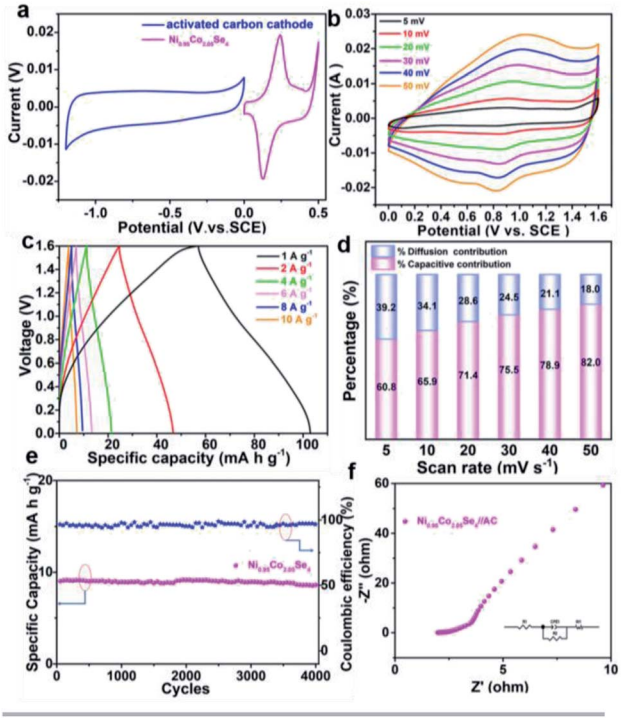

Fig. 5 (a) Comparison of CV curves for the activated carbon cathode and $Ni_{0.95}Co_{2.05}Se_4$ anode at a scan rate of 5 mV s^{-1}, (b) CV curves of the $Ni_{0.95}Co_{2.05}Se_4$ material at various scan rates, (c) GCD curves of the $Ni_{0.95}Co_{2.05}Se_4$ material under various current densities, (d) process contribution graph. (e) Cycle performance of the $Ni_{0.95}Co_{2.05}Se_4$ electrodes in the HSC. (f) Nyquist plots; the inset is the fitting equivalent electrical circuit model.

material is polarized and damaged for oxygen evolution reaction as shown in Fig. S11b,† therefore, a suitable voltage window of 0–1.6 V was selected for $Ni_{0.95}Co_{2.05}Se_4$//AC device. Fig. 5b and Fig. S13† show the CV curves of the $Ni_{0.95}Co_{2.05}Se_4$//AC and other HSCs at various scan rates, respectively. The current response gradually increases with the rise of the scan rates, and a little redox peak position was found to be stable at 0.85 and 1.1 V. The charges storage mechanism of $Ni_{0.95}Co_{2.05}Se_4$//AC HSC was also characterized by CV technique at the scan speed of 5–50 mV s^{-1}, the calculated value of b is 0.897 (Fig. S14†), it shows that the process is major dominated by surface capacitive control and involved in diffusion-controlled behavior. In order to compare the contribution ratios of the two behaviors at different scan rate, the calculated results were shown in Fig. 5d. The pseudocapacitive property increases from 60.8% to 82% with increase the scan rate from 5 to 50 mV s^{-1}, indicating the capacitive contribution is participating in charge storage at high rate for $Ni_{0.95}Co_{2.05}Se_4$//AC HSC. The charging–discharging voltage profiles of the $Ni_{0.95}Co_{2.05}Se_4$//AC HSC and other HSCs at a series of current densities from 1 to 10 A g^{-1} are approximately symmetric (Fig. 5c and S15†), which manifests the special nature of the excellent coulombic efficiency and superior electrochemical reversibility. The specific capacitance of $Ni_{0.95}Co_{2.05}Se_4$//AC HSC calculated from the discharge time is 45.9 mA h g^{-1} at 1 A g^{-1}, and it still maintains 34.2 mA h g^{-1} at

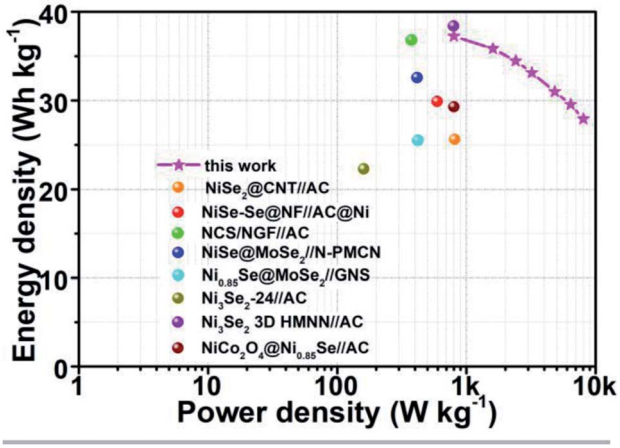

Fig. 6 Ragone plot the assembled $Ni_{0.95}Co_{2.05}Se_4$//AC ASC supercapacitor and other related supercapacitors.

10 A g^{-1}. The impedance diagram of the HSC is shown in Fig. 5f, the fitting result of R_s and R_{ct} is 2.961 Ω and 1.831 Ω, respectively. The cycling performance of $Ni_{0.95}Co_{2.05}Se_4$//AC HSC was further investigated by repeated GCD tests at 4 A g^{-1} (Fig. 5e). The specific capacity $Ni_{0.95}Co_{2.05}Se_4$//AC HSC retains 95.21% of the initial capacity and coulomb efficiency keeps 96.71% after 4000 cycles, respectively, suggesting that the constructed HSC possesses superior long-term electrochemical stability.

In practical applications, energy density and power density are two important factors that determine the quality of energy storage equipment. Fig. 6 shows the energy density and power density of the assembled $Ni_{0.95}Co_{2.05}Se_4$//AC HSC and other related supercapacitor devices. By comparison, the specific energy/power densities of our constructed $Ni_{0.95}Co_{2.05}Se_4$//AC HSC is no less than or even better than the previous related ASC devices. The corresponding devices are NiSe–Se@NF//AC@Ni (29.9 W h kg^{-1} at 594.46 W kg^{-1}),[41] NCS/NGF//AC (36.8 W h kg^{-1} at 375 W kg^{-1}),[42] NiSe@$MoSe_2$//N-PMCN (32.6 W h kg^{-1} at 415 W kg^{-1}),[43] $Ni_{0.85}Se$@$MoSe_2$//GNS (25.5 W h kg^{-1} at 420 W kg^{-1}),[44] Ni_3Se_2-24//AC (22.3 W h Kg^{-1} at 160.4 W kg^{-1}),[32] $NiSe_2$@CNT//AC (25.61 W h kg^{-1} at 810 W kg^{-1}),[45] $NiCo_2O_4$@$Ni_{0.85}Se$//AC (29.3 W h kg^{-1} at 799 W kg^{-1}),[46] Ni_3Se_2 3D HMNN//AC (38.4 W h kg^{-1} at 794.5 W kg^{-1}).[37] These above results suggest that the $Ni_{0.95}Co_{2.05}Se_4$//C device possesses remarkable energy storage capability and cycling stability, which demonstrate greatly practical applications in energy storage devices.

4. Conclusion

In summary, a series of $Ni_xCo_{3-x}Se_4$ particles with high electrochemical capacitance were synthesized with a simple and effective solvothermal method. The optimized $Ni_{0.95}Co_{2.05}Se_4$ electrode specific capacitance can reach 1038.75 F g^{-1} at 1 A g^{-1}, which is higher than the other four samples. The $Ni_{0.95}Co_{2.05}Se_4$ electrode has excellent rate capability as well as outstanding cycling stability. The best electrochemical performance of $Ni_{0.95}Co_{2.05}Se_4$ may be ascribed to its high surface area, low charge transfer resistance, and high diffusion coefficient in the series samples. Furthermore, an HSC device is assembled by using activated carbon as the negative electrode and $Ni_{0.95}Co_{2.05}Se_4$ as the positive electrode, which present excellent stability and high coulomb efficiency during the 4000 cycles. Moreover, the $Ni_{0.95}Co_{2.05}Se_4$//AC HSC arrives an energy density of 37.22 W h kg^{-1} and a power density of 800.90 W kg^{-1}. The ASC device can keep 95.21% of original capacity after 4000 cycles. The electrochemical properties indicate the $Ni_{0.95}Co_{2.05}Se_4$ is a promising electrode in future energy storage devices.

Conflicts of interest

There are no conflicts to declare.

Acknowledgements

This work was supported by the National Science Foundation of China (No. 21603004, U1604119), the Key Scientific Project of Higher Education of Henan Province (No. 22A150002), and the Program for Innovative Research Team of Science and Technology in the University of Henan Province (18IRTSTHN006).

Notes and references

1 X. Y. Yu and X. W. Lou, Mixed Metal Sulfides for Electrochemical Energy Storage and Conversion, *Adv. Energy Mater.*, 2018, **8**, 1701592.
2 Y. Zhang, Q. Zhou, J. X. Zhu, Q. Y. Yan, S. X. Dou and W. P. Sun, Nanostructured Metal Chalcogenides for Energy Storage and Electrocatalysis, *Adv. Funct. Mater.*, 2017, **27**, 1702317.
3 Q. B. Yun, Q. P. Lu, X. Zhang, C. L. Tan and H. Zhang, Three-Dimensional Architectures Constructed from Transition-Metal Dichalcogenide Nanomaterials for Electrochemical Energy Storage and Conversion, *Angew. Chem., Int. Ed.*, 2018, **57**, 626–646.
4 Y. H. Dou, L. Zhang, X. Xu, Z. Q. Sun, T. Liao and S. X. Dou, Atomically thin non-layered nanomaterials for energy storage and conversion, *Chem. Soc. Rev.*, 2017, **46**, 7338–7373.
5 Y. Li, Y. X. Xu, W. P. Yang, W. X. Shen, H. G. Xue and H. Pang, MOF-Derived Metal Oxide Composites for Advanced Electrochemical Energy Storage, *Small*, 2018, **14**, 1704.
6 Y. Gogotsi and R. M. Penner, Energy Storage in Nanomaterials-Capacitive, Pseudocapacitive, or Battery-like?, *ACS Nano*, 2018, **12**, 2081–2083.
7 T. Brousse, D. Bélanger and J. W. Longd, To Be or Not To Be Pseudocapacitive?, *J. Electrochem. Soc.*, 2015, **162**, A5185–A5189.
8 J. L. Qi, Y. T. Yan, Y. F. Cai, J. Cao and J. C. Feng, Nanoarchitectured Design of Vertical-Standing Arrays for Supercapacitors: Progress, Challenges, and Perspectives, *Adv. Funct. Mater.*, 2021, **31**, 2006030.
9 Y. L. Shao, M. F. El-Kady, J. Y. Sun, Y. G. Li, Q. H. Zhang, M. F. Zhu, H. Z. Wang, B. Dunn and R. B. Kaner, Design

and Mechanisms of Asymmetric Supercapacitors, *Chem. Rev.*, 2018, **118**, 9233–9280.

10 R. Lei, H. W. Ni, R. S. Chen, H. Z. Gu, H. Zhang and S. Dong, *In situ* growth of self-supported and defect-engineered carbon nanotube networks on 316L stainless steel as binder-free supercapacitors, *J. Colloid Interface Sci.*, 2018, **532**, 622–629.

11 R. Lei, H. Zhang, Q. Fang, H. W. Ni and H. Z. Gu, MnO_2 nanowires electrodeposited on freestanding graphenated carbon nanotubes as binder-free electrodes with enhanced supercapacitor performance, *Mater. Lett.*, 2019, **249**, 140–142.

12 R. Lei, J. H. Gao, L. F. Qi, L. L. Ye, C. Wang, Y. Le, Y. Huang, X. G. Shi and H. W. Ni, Construction of MnO_2 nanosheets@graphenated carbon nanotube networks core–shell heterostructure on 316L stainless steel as binderfree supercapacitor electrodes, *Int. J. Hydrogen Energy*, 2020, **45**, 28930–28939.

13 H. J. Zhou, X. X. Li, Y. Li, M. B. Zheng and H. Pang, Applications of M_xSe_y (M = Fe, Co, Ni) and Their Composites in Electrochemical Energy Storage and Conversion, *Nano-Micro Lett.*, 2019, **11**(40), 1–33.

14 T. T. Nguyen, J. Balamurugan, V. Aravindan, N. H. Kim and J. H. Lee, Boosting the Energy Density of Flexible Solid-State Supercapacitors *via* Both Ternary NiV_2Se_4 and $NiFe_2Se_4$ Nanosheet Arrays, *Chem. Mater.*, 2019, **31**, 4490–4504.

15 X. Song, C. Huang, Y. Qin, H. Li and H. C. Chen, Hierarchical hollow, sea-urchin-like and porous $Ni_{0.5}Co_{0.5}Se_2$ as advanced battery material for hybrid supercapacitors, *J. Mater. Chem. A*, 2018, **6**, 16205–16212.

16 L. R. Hou, Y. Y. Shi, C. Wu, Y. R. Zhang, Y. Z. Ma, X. Sun, J. F. Sun, X. G. Zhang and C. Z. Yuan, Monodisperse Metallic $NiCoSe_2$ Hollow Sub-Microspheres: Formation Process, Intrinsic Charge-Storage Mechanism, and Appealing Pseudocapacitance as Highly Conductive Electrode for Electrochemical Supercapacitors, *Adv. Funct. Mater.*, 2018, **28**, 1705921.

17 H. Mei, L. Zhang, K. Zhang, J. Gao, H. Zhang, Z. Huang, B. Xu and D. Sun, Conversion of MOF into carbon-coated $NiSe_2$ yolk–shell microspheres as advanced battery-type electrodes, *Electrochim. Acta*, 2020, **357**, 136866.

18 S. Wang and S. Ma, Facile fabrication of $Ni_{0.85}Se$ nanowires by the composite alkali salt method as a novel cathode material for asymmetric supercapacitors, *Dalton Trans.*, 2019, **48**, 3906–3913.

19 X. Li, H. Wu, C. Guan, A. M. Elshahawy, Y. Dong, S. J. Pennycook and J. Wang, (Ni,Co)Se_2/NiCo-LDH core/shell structural electrode with the cactus-Like (Ni,Co)Se_2 core for asymmetric supercapacitors, *Small*, 2019, **15**, 1803895.

20 B. G. Amin, J. Masud and M. Nath, Facile one-pot synthesis of $NiCo_2Se_4$-rGO on Ni foam for high performance hybrid supercapacitors, *RSC Adv.*, 2019, **9**, 37939–37946.

21 Y. L. Liu, C. Yan, G. G. Wang, F. Li, Q. Kang, H. Y. Zhang and J. C. Han, Selenium-rich nickel cobalt bimetallic selenides with core–shell architecture enable superior hybrid energy storage devices, *Nanoscale*, 2020, **12**, 4040–4050.

22 Z. Y. Xie, D. P. Qiu, J. N. Xia, J. Y. Wei, M. Li, F. Wang and R. Yang, Hollow Biphase Cobalt Nickel Perselenide Spheres Derived from Metal Glycerol Alkoxides for High-Performance Hybrid Supercapacitors, *ACS Appl. Mater. Interfaces*, 2021, **13**, 12006–12015.

23 Y. Wang, W. Zhang, X. Guo, K. Jin, Z. Chen, Y. Liu, L. Yin, L. Li, K. Yin, L. Sun and Y. Zhao, Ni–Co selenide nanosheet/3D graphene/nickel foam binder-free electrode for high-performance supercapacitor, *ACS Appl. Mater. Interfaces*, 2019, **11**, 7946–7953.

24 M. M. Vadiyar, S. B. Bandgar, S. S. Kolekar, J.-Y. Chang, Y.-C. Ling, Z. Ye and A. V. Ghule, Holey C@$ZnFe_2O_4$ Nanoflakes by Carbon Soot Layer Blasting Approach for High Performance Supercapacitors, *ACS Appl. Energy Mater.*, 2019, **2**, 6693–6704.

25 X. Zhou, J. Zhu, Y. Lu, Y. Zhang, Y. Hong, W. Wang, K. Karimov, I. Murtaza, Q. Wang and X. Dong, Three-Dimensional Co–S–P Nanoflowers as Highly Stable Electrode Materials for Asymmetric Supercapacitors, *ACS Sustainable Chem. Eng.*, 2019, **7**, 11448–11454.

26 A. Ray, A. Roy, P. Sadhukhan, S. R. Chowdhury, P. Maji, S. K. Bhattachrya and S. Das, Electrochemical properties of TiO_2–V_2O_5 nanocomposites as a high performance supercapacitors electrode material, *Appl. Surf. Sci.*, 2018, **443**, 581–59122.

27 Y. Xiao, W. Wei, M. Zhang, S. Jiao, Y. Shi and S. Ding, Facile Surface Properties Engineering of High-Quality Graphene: Toward Advanced Ni-MOF Heterostructures for High-Performance Supercapacitor Electrode, *ACS Appl. Energy Mater.*, 2019, **2**, 2169–2177.

28 F. Javier García-García, A.-K. Larsson, L. Norèn and R. L. Withers, The crystal structures of Co_3Se_4 and Co_7Se_8, *Solid State Sci.*, 2004, **6**, 725–733.

29 H. Chen, M. Fan, C. Li, G. Tian, C. Lv, D. Chen, K. Shu and J. Jiang, One-pot synthesis of hollow NiSe–CoSe nanoparticles with improved performance for hybrid supercapacitors, *J. Power Sources*, 2016, **329**, 314–322.

30 Y. Wang, W. Zhang, X. Guo, K. Jin, Z. Chen, Y. Liu, L. Yin, L. Li, K. Yin, L. Sun and Y. Zhao, Ni–Co Selenide Nanosheet/3D Graphene/Nickel Foam Binder-Free Electrode for High-Performance Supercapacitor, *ACS Appl. Mater. Interfaces*, 2019, **11**, 7946–7953.

31 J. Yang, Z. Sun, J. Wang, J. Zhang, Y. Qin, J. You and L. Xu, Hierarchical $NiSe_2$ spheres composed of tiny nanoparticles for high performance asymmetric supercapacitors, *CrystEngComm*, 2019, **21**, 994–1000.

32 L. Zhao, P. Zhang, Y. Zhang, Z. Zhang, L. Yang and Z.-G. Chen, Facile synthesis of hierarchical Ni_3Se_2 nanodendrite arrays for supercapacitors, *J. Mater. Sci. Technol.*, 2020, **54**, 69–76.

33 Y. Hu, C. Huang, S. Jiang, Y. Qin and H. C. Chen, Hierarchical nickel–cobalt selenide nanoparticles/nanosheets as advanced electroactive battery materials for hybrid supercapacitors, *J. Colloid Interface Sci.*, 2020, **558**, 291–300.

34 S. Li, Y. Ruan and Q. Xie, Morphological modulation of $NiCo_2Se_4$ nanotubes through hydrothermal selenization for

asymmetric supercapacitor, *Electrochim. Acta*, 2020, **356**, 136837.

35 M. Sakthivel, S. Ramaraj, S.-M. Chen and K.-C. Ho, Bimetallic vanadium cobalt diselenide nanosheets with additional active sites for excellent asymmetric pseudocapacitive performance: comparing the electrochemical performances with M–$CoSe_2$ (M = Zn, Mn, and Cu), *J. Mater. Chem. A*, 2019, **7**, 12565–12581.

36 L. Du, W. Du, H. Ren, N. Wang, Z. Yao, X. Shi, B. Zhang, J. Zai and X. Qian, Honeycomb-like metallic nickel selenide nanosheet arrays as binder-free electrodes for high-performance hybrid asymmetric supercapacitors, *J. Mater. Chem. A*, 2017, **5**, 22527–22535.

37 Y. Liu, Q. Xu, R. Wang, Y. Zheng, L. Zhu, Z. Wang and W. Zheng, Ionothermal synthesis of three-dimensional hierarchical Ni_3Se_2 mesoporous nanosheet networks with enhanced performance for asymmetric supercapacitors, *J. Mater. Chem. A*, 2020, **8**, 797–809.

38 L. Li, L. Jiang, Y. Qing, Y. Zeng, Z. Zhang, L. Xiao, X. Lu and Y. Wu, Manipulating nickel oxides in naturally derived cellulose nanofiber networks as robust cathodes for high-performance Ni–Zn batteries, *J. Mater. Chem. A*, 2020, **8**, 565–572.

39 S. Lalwani, S. Karade, J. H. Eum and H. Kim, Maximizing Redox Charge storage *via* Cation(V)–Anion(S) Dual-Doping on Nickel Diselenide Nanodiscs for Hybrid Supercapacitors, *ACS Appl. Energy Mater.*, 2021, **4**, 2430–2439.

40 A. Ray, A. Roy, S. Saha, M. Ghosh, S. R. Chowdhury, T. Maiyalagan, S. K. Bhattacharya and S. Das, Electrochemical energy storage properties of Ni–Mn-Oxide electrodes for advance asymmetric supercapacitor application, *Langmuir*, 2019, **35**, 8257–8267.

41 S. Subhadarshini, E. Pavitra, G. S. Rama Raju, N. R. Chodankar, D. K. Goswami, Y. K. Han, Y. S. Huh and N. C. Das, One-Dimensional NiSe–Se Hollow Nanotubular Architecture as a Binder-Free Cathode with Enhanced Redox Reactions for High-Performance Hybrid Supercapacitors, *ACS Appl. Mater. Interfaces*, 2020, **12**, 29302–29315.

42 Y. Chen, T. Liu, L. Zhang and J. Yu, $NiCo_2S_4$ Nanotubes Anchored 3D Nitrogen-Doped Graphene Framework as Electrode Material with Enhanced Performance for Asymmetric Supercapacitors, *ACS Sustainable Chem. Eng.*, 2019, **7**, 11157–11165.

43 H. Peng, J. Zhou, K. Sun, G. Ma, Z. Zhang, E. Feng and Z. Lei, High- Performance Asymmetric Supercapacitor Designed with a Novel NiSe@$MoSe_2$ Nanosheet Array and Nitrogen-Doped Carbon Nanosheet, *ACS Sustainable Chem. Eng.*, 2017, **5**, 5951–5963.

44 H. Peng, C. D. Wei, K. Wang, T. Y. Meng, G. F. Ma, Z. Q. Lei and X. Gong, $Ni_{0.85}Se$@ $MoSe_2$ Nanosheet Arrays as the Electrode for High-Performance Supercapacitors, *ACS Appl. Mater. Interfaces*, 2017, **9**, 17067–17075.

45 Y. Zheng, Y. Tian, S. Sarwar, J. Luo and X. Zhang, Carbon nanotubes decorated $NiSe_2$ nanosheets for high-performance supercapacitors, *J. Power Sources*, 2020, **452**, 227793.

46 Y. Sui, A. Ye, J. Qi, F. Wei, Y. He, Q. Meng, Y. Ren and Z. Sun, Construction of $NiCo_2O_4$@$Ni_{0.85}Se$ core–shell nanorod arrays on Ni foam as advanced materials for an asymmetric supercapacitor, *J. Alloys Compd.*, 2019, **778**, 234–238.